Research Square

Preprints are preliminary reports that have not undergone peer review.
They should not be considered conclusive, used to inform clinical practice,
or referenced by the media as validated information.

# Additive Manufacturing of Hydrogel-Polymer Combinations for Applications in Smart Reactors

**Jan Hünting**

jan.huenting@tuhh.de

Hamburg University of Technology: Technische Universitat Hamburg https://orcid.org/0009-0000-7484-4992

**Kathrin Marina Eckert**
**Jelle Jacobs**
**Maria Isabelle Maiwald**
**Dirk Herzog**
**Irina Smirnova**
**Michael Schlüter**
**Ingomar Kelbassa**

**Research Article**

**Keywords:**

**Posted Date:** November 9th, 2026

**DOI:** https://doi.org/10.21203/rs.3.rs-11284508/v1

**License:** This work is licensed under a Creative Commons Attribution 4.0 International License.
Read Full License

# Additive Manufacturing of Hydrogel-Polymer Combinations for Applications in Smart Reactors


| | |
|---|---|
| Jan Hünting[1,*], | ORCID 0009-0000-7484-4992 |
| Kathrin Marina Eckert[2,3], | ORCID 0000-0002-8454-4886 |
| Jelle Jacobs[1], | ORCID 0009-0007-6893-1281 |
| Maria Isabelle Maiwald[1], | ORCID 0000-0001-9719-8057 |
| Dirk Herzog[1,4], | ORCID 0000-0001-7059-6151 |
| Irina Smirnova[2,3], | ORCID 0000-0003-4503-4039 |
| Michael Schlüter[5], | ORCID 0000-0001-5969-2150 |
| Ingomar Kelbassa[1,4], | ORCID 0009-0003-1325-4472 |

[1]Institute for Industrialization of Smart Materials (ISM), Hamburg University of Technology (TUHH), Harburger Schloßstraße 28, 21079 Hamburg, Germany

[2]Institute of Thermal Separation Processes (TVT), Hamburg University of Technology (TUHH), Eißendorfer Straße 38, 21073 Hamburg, Germany

[3]United Nations University Hub on Engineering to Face Climate Change at the Hamburg University of Technology, United Nations University Institute for Water, Environment and Health (UNU-INWEH), Hamburg, Germany

[4]Fraunhofer Research Institution for Additive Manufacturing Technologies (IAPT), Am Schleusengraben 14, 21029 Hamburg, Germany

[5]Institute of Multiphase Flows (IMS), Hamburg University of Technology (TUHH), Eißendorfer Straße 38, 21073 Hamburg, Germany

***Corresponding author:** Jan Hünting, +49 40 30601-4422, jan.huenting@tuhh.de

## Nomenclature

| Abbreviation | Definition |
|---|---|
| AM | Additive manufacturing |
| DoE | Design of experiments |
| $HG_{hwc}$ | Hydrogel formulation containing 10 wt% water |
| $HG_{lwc}$ | Hydrogel formulation containing 7.5 wt% water |
| MEX/P | Material extrusion of polymers |
| POCS | Periodic open-cell structures |
| RSM | Response surface methodology |
| SDS | Supplementary dataset of this paper |
| TPU | Thermoplastic polyurethane |
| UV | Ultraviolet |
| 3D | Three-dimensional |

| Symbol/ variable | Definition | Unit |
|---|---|---|
| EM | Extrusion multiplier | - |
| PS | Printing speed | mm $s^{-1}$ |
| r | Fitted radius of curvature | mm |
| $R^2_{adj}$ | Adjusted coefficient of determination | % |
| $R^2_{pred}$ | Predicted coefficient of determination | % |
| RMSE/r | Normalized root-mean-square error of the circular fit | - |
| $V/V_0$ | Normalized hydrogel monolith volume | - |
| $\kappa$ | Signed specimen curvature | $mm^{-1}$ |
| $\Delta\kappa$ | Change in signed specimen curvature | $mm^{-1}$ |


## Abstract

The increasing use of renewable raw materials with fluctuating properties creates a need for process equipment that can adapt to changing operating conditions. As components of smart reactors, self-adaptive structures could respond to reaction conditions such as temperature, pressure drop, or pH to maintain selectivity and yield within a desired range. Stimuli-responsive hydrogels are promising materials as they undergo reversible swelling and shrinkage when exposed to external stimuli, thereby enabling changes in reactor geometry and flow conditions. However, their low mechanical stability limits their use as structural reactor elements. This paper therefore proposes a multi-material additive manufacturing approach combining material extrusion of thermoplastics with a second extrusion system for hydrogel precursor. Hydrogel formulations with different water contents are investigated regarding printability and curing behavior, and response surface methodology is used to identify a robust processing parameter set. The selected formulation exhibits an average mass-based shrinkage of 54.22 ± 3.36% between 25 and 40 °C, while image-based measurements show that the majority of the volume change occurs within the first 5–10 min, with an apparent volumetric plateau reached after 16–18 min. Thermoresponsive actuation is further demonstrated using hydrogel-thermoplastic polyurethane bilayer specimens, with all specimens exhibiting a complete reversal in bending direction and curvature changes between 0.0343 and 0.0550 $mm^{-1}$. Based on these results, potential hydrogel-polymer design elements for smart reactors are proposed, including adaptive baffles, variable flow cross-sections, flow redirecters, and adaptive structured reactor internals.



**Keywords:** Additive Manufacturing, Material Extrusion, Hydrogels, Polymers, Multi-material, Smart Reactors

## 1. Introduction

Stimuli-responsive hydrogels [1] are three-dimensional (3D) polymeric networks that exhibit a very high water content (up to 99% of the overall weight). These materials are able to swell or shrink considerably (more than ten times in volume) upon an external stimulus, for example, temperature, light, or pH [2]. As swelling and shrinkage are reversible, stimuli-responsive hydrogels allow for the design of actuators with different types of movement [3].

Additive Manufacturing (AM) offers superior design freedom, enabling the fabrication of complex 3D geometries due to its layer-by-layer operation principle [4] and is thus a promising manufacturing approach in the context of smart reactors for the creation of more complex actuator designs. For the printing of hydrogels, Vat Photopolymerization (VPP as per ISO/ASTM 52900 [5]) has successfully been used [6]. In VPP, a light source is employed to selectively cure photoreactive resins. The manufacturing system consists of a vat filled with liquid resin, in which a light source such as a laser or a digital light projector induces polymerization in a layer-wise manner. After photopolymerization, the build plate is incrementally repositioned, enabling fresh resin to flow over the previously solidified layer [7]. The potential of AM for tailoring both the macroscopic geometry and responsive behavior of hydrogel structures has been shown in previous studies. Hu et al. [8] fabricated stimuli-responsive periodic open-cell structures (POCS) for use as adaptive packings in multiphase flow systems, demonstrating that larger hydrogel structures can be employed to alter fluid-dynamic properties and mass transfer through stimulus-induced geometric changes. Liu et al. [9], in contrast, used 3D-printed hierarchical porosity in PNIPAM structures to enhance water transport and thereby accelerate temperature-induced swelling and deswelling kinetics.

While VPP is typically restricted to one material per build, several multi-material VPP approaches, such as multiple vat switching, dynamic fluid delivery, or vat-less approaches using local ink deposition are reported in literature [10]. However, these methods appear rather complex and are restricted to the use of photocurable resins with limited range of material properties. A hybrid approach combining VPP with Material Extrusion of Polymers (MEX/P as per ISO/ASTM 52900 [5], often also referred to as Fused Deposition Modeling FDM, and Fused Filament Fabrication FFF) is reported by Cheng et al. [11] for specific material combinations, but not including hydrogels.

MEX/P is the most common industrial polymer AM technology with an installed base of > 100,000 industrial systems worldwide in 2025 [12]. In MEX/P, the object is manufactured by the selective deposition of molten thermoplastic material. The polymer, typically supplied as a filament wound onto spools, is heated and extruded through a nozzle onto a build plate to fabricate the object layer by layer based on a digital model [13]. Common materials include Acrylonitrile Butadiene Styrene (ABS), Polyamide 6 (PA6), Polypropylene (PP), Polylactide (PLA), and Glycol-modified Polyethylene Terephthalate (PETG) [14]. Among thermoplastic elastomers, thermoplastic Polyurethane (TPU) is available for MEX/P [15].

With regard to hydrogels, printing by extrusion is also reported in literature [16], where the hydrogel or hydrogel-forming polymer is typically extruded through a syringe. Kirchmajer et al. [17] discuss the extrusion printing of hydrogel-forming polymers for tissue engineering applications. Koltsov et al. [18] adapted a commercial MEX/P printer for printing hydrogel precursors through a syringe. Two printing modes were realized, droplet printing of microspheres with a diameter of 100 µm and a distance between spheres of 200 µm, as well as filament printing of lines with a thickness between 300 µm and 2 mm. Lattice-type shapes were demonstrated with this printer. Another similar syringe-based printer is reported by

Zhou et al. [19]. Imrie and Jin [20] use a multi-nozzle photocuring 3D printer to fabricate reversible addition-fragmentation chain transfer polymer network hydrogels alongside standard free-radical polymerized hydrogels. The bilayer material shows bending behavior due to differences in the swelling behavior of the individual components when placed in water. Furthermore, Hu et al. [21] report the successful MEX/P of a rigid reactor structure from PLA while filling it in situ with a responsive hydrogel acting within a valve.

Hydrogels are very soft, with Young's moduli in the range of brain tissue [22]. Because of their softness, responsive hydrogel structures are best used as actuators between harder polymeric components in smart reactors. Examples of this reactor type include multipurpose reactors that sustainably convert renewable resources into different products and self-adapting reactors that operate autonomously [23]. Therefore, this paper presents an innovative approach for a combined material extrusion of hydrogel precursors and thermoplastic polymers, proposing a specific printer setup, followed by a discussion of the individual material printing characteristics as well as their adhesion to each other. For a selected combination, the actuation behavior of the structures is investigated. Based on these results, several potential design elements are proposed for integration into smart reactors. Stimuli-induced geometric changes could thereby enable adaptive control of flow distribution [21], catalytic performance [24], and mixing behavior [25], while also providing a potential means of adjusting local residence times.

## 2. Multi-Material Extrusion 3D Printer

The printer used in this study is based on a Voron Trident 300 × 300 × 300 Rev. C self-assembly kit, manufactured by LDO Motors (Shenzhen, China) and sold by meltbro (Bonn, Germany). The printer is equipped with a structured build plate measuring 300 mm × 300 mm. Self-printed parts are manufactured from ABS and the printer is expanded upwards to make room for the second extruder. The error-prone inductive sensor for the calibration is replaced with a Klicky probe and Mainsail is implemented as web-browser-based control interface.

For the extension to a hydrogel-polymer multi-material 3D printer, the vipro-HEAD 3 from ViscoTec (Töging am Inn, Germany) is integrated as a second extrusion head. This system is based on a progressive cavity pump principle, allowing the precise extrusion of liquids such as hydrogel precursors, and is referred to as the precursor extruder hereafter. The extruder mount is vertically actuated by an electric motor to adjust the nozzle-to-build-plate distance. This is necessary for 3D printing with liquid material, since the precursor cannot be mechanically leveled during deposition as it is done with molten thermoplastic material in the MEX/P process. The precursor is stored in a reservoir and is fed by gravity to the extruder.

The ultraviolet (UV) ringlight RL81-75 UV from StarLight Opto-Electronics (Nürnberg, Germany) is mounted around the precursor extruder for the uniform in situ photopolymerization of the extruded precursor. It provides UV light from eight light-emitting diodes (LED) with a wavelength of 365 nm and adjustable intensity. In this study, relative irradiance values, expressed as percentages, were compared. The lamp-to-specimen distance is measured to be 45 mm. To prevent premature polymerization of the precursor before its deposition, a shadow-casting shield is designed and attached around the nozzle (Fig. 4). For improved user safety, the whole printer is fully enclosed in aluminum sheets, a UV-protective window (protection level LB6 according to DIN EN 12254 [26] and DIN EN 207 [27]) is integrated into the front door, and UV safety glasses must be worn. In addition, a safety system is developed that prevents the printer door from being opened while the UV lamp is on and prevents the lamp from being turned on while the door is open. The system uses a hardwired relay-based control system, an electromagnetic door lock,

and a footswitch for manual unlocking. The printer setup with its most important components is shown in Fig. 1.

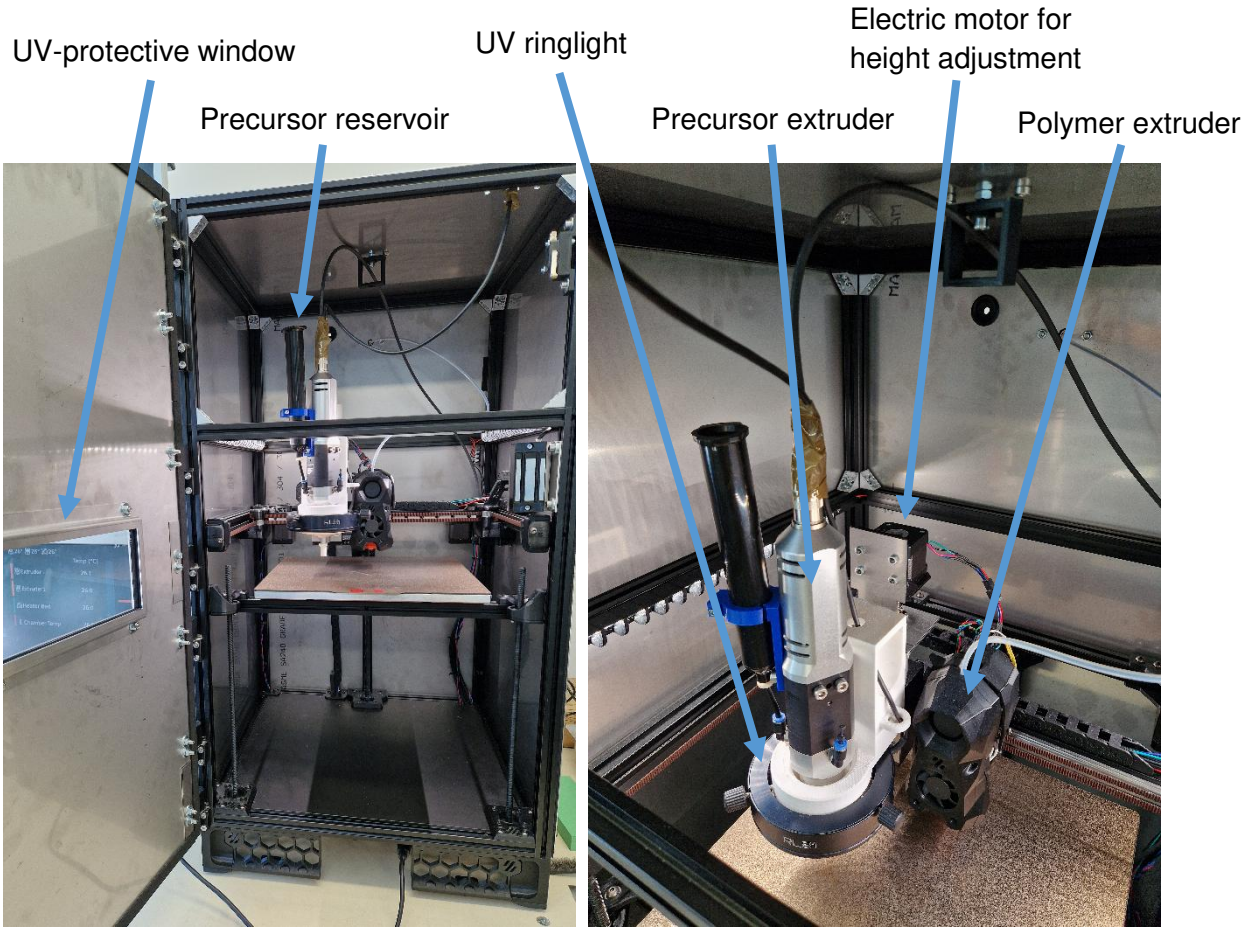



**Fig. 1** Multi-material 3D printing setup combining thermoplastic extrusion and hydrogel precursor deposition (300 mm × 300 mm build plate shown for scale)

The printer firmware is modified to implement the precursor extruder and to prevent collisions by limiting the available travel range in the X and Y directions. Furthermore, the electric motor controlling the precursor extruder height is incorporated, and the bed leveling and mesh calibration points are adjusted according to the reduced printable area.

## 3. Materials and Methods

### 3.1. Materials

#### 3.1.1. Hydrogels

The thermoresponsive hydrogel formulations consist of 1-phenylazo-2-naphthol (Sudan I, Sigma-Aldrich, >95%), lithium phenyl-2,4,6-trimethylbenzoylphosphinate (LAP, BLDpharm, 97%), *N,N'*-methylenebisacrylamide (MBA, Sigma-Aldrich, 99%), *N*-isopropylacrylamide (NIPAM, Abcr GmbH, >98%), poly(ethylene glycol) (PEG, Sigma-Aldrich, $M_n$ = 400 g/mol), and deionized water. Thermoresponsive behavior originates from the cross-linked poly(*N*-isopropylacrylamide) network. The formulation was tested with two different water contents, 10 wt% water ($HG_{hwc}$, high water content) and 7.5 wt% water ($HG_{lwc}$, low water content), to investigate the influence of water content and the associated expected changes in flow behavior on printability (see subsection 3.2.2 for further information). Table 1 lists all constituents of both formulations together with their

absolute quantities and weight percentages in brackets. The precursor components were mixed and dissolved in an ultrasonic bath for at least 8 h.

**Table 1** Absolute quantities and weight percentages of all hydrogel precursor components

| Formulation | $HG_{hwc}$ | $HG_{lwc}$ |
|---|---|---|
| **Sudan I [g (wt%)]** | 0.0145 (0.029) | 0.0145 (0.029) |
| **LAP [g (wt%)]** | 0.1756 (0.351) | 0.1817 (0.363) |
| **MBA [g (wt%)]** | 2.0299 (4.059) | 2.0846 (4.165) |
| **NIPAM [g (wt%)]** | 9.0073 (18.009) | 9.2584 (18.499) |
| **PEG [g (wt%)]** | 33.7799 (67.541) | 34.7619 (69.456) |
| **Water [g (wt%)]** | 5.0070 (10.011) | 3.7477 (7.488) |

#### 3.1.2. Thermoplastic Polymer

The thermoplastic polymer in this study was intended to act as a mechanically stable base structure for the soft hydrogel while remaining sufficiently flexible to be deformed by the thermoresponsive hydrogel. Therefore, the commercially available Extrudr Flex Medium TPU filament from the company FD3D (Lustenau, Austria) was chosen. It has a diameter of 1.75 mm, and a tensile modulus of 40 MPa. The Shore A hardness of 98 offers a compromise between flexibility and structural stability. Before each use, the filament was dried in the filament dryer Space Pi Dryer from Creality 3D Technology (Shenzhen, China) for 6 h at 55 °C.

### 3.2. Methodology

#### 3.2.1. Print Preparation

All digital models used in this paper were designed with Inventor Professional 2024 from Autodesk (San Francisco, USA). Slicing and G-code generation were performed with the open-source software SuperSlicer version 2.5.59.13. The precursor extruder was configured in the slicer software as a second extruder and its offsets in the X and Y directions from the first extruder were determined experimentally during initial calibration. Before each day of printing, the build plate was leveled and the nozzle-to-bed distance was calibrated. After printing, the precursor reservoir was emptied and cleaned, and the extruder was flushed with water to prevent residual precursor from curing inside the system. For a continuous and even extrusion, both materials were primed and both nozzles were cleaned prior to each print job.

#### 3.2.2. Preliminary Studies

Preliminary studies were conducted to identify relevant process parameters and their upper and lower bounds of interest for the following investigations. Tests on the water content of the hydrogel formulations ranging from 0 to 20 wt% showed that water contents below 7.5 wt% led to the formation of large amounts of crystallized threads (pictures in supplementary dataset (SDS) [28]), whereas water contents above 10 wt% produced hydrogel precursors with insufficient mechanical stability to retain their shape after deposition. Printing speed (PS) and extrusion multiplier (EM) were identified as the relevant process parameters, and their bounds for the subsequent design of experiments (DoE) were selected to cover the practically printable process window, including threshold conditions. Additional experiments demonstrated that variations in build plate temperature, UV lamp intensity, nozzle diameter, and nozzle-to-bed distance either had no

substantial influence within the tested range or yielded a clearly preferred operating condition. These parameters were therefore kept constant throughout the study and excluded from the DoE. The values of these parameters are shown in Table 2.

**Table 2** Fixed process parameters for the DoE specimen manufacturing

| Process parameter | Unit | Value |
|---|---|---|
| **Build plate heating** | °C | off |
| **UV lamp intensity** | % | 100 |
| **Nozzle diameter** | mm | 0.33 |
| **Nozzle-to-bed distance** | mm | 0.33 |

### 3.2.3. Hydrogel Design of Experiments

To systematically evaluate the influence of the printing parameters on hydrogel precursor track geometry and curing behavior and to identify a robust parameter set for the fabrication of dimensionally accurate single tracks, a response surface methodology (RSM) was applied. Two identical DoEs were conducted separately for hydrogel formulations with different water contents instead of including the water content as an additional factor. This approach was chosen because the preparation of hydrogel formulations with numerous intermediate water contents is labor-intensive and associated with limited reproducibility. The software Statgraphics Centurion 19 from Statgraphics Technologies (The Plains, USA) was used to implement the RSM for hydrogel precursor single tracks with a target size of 0.5 mm × 0.2 mm × 50 mm. Four response variables to be examined were defined based on the results of the preliminary studies. The response variables, their corresponding optimization goals, and the geometric target values are summarized in Table 3.

**Table 3** Specified response variables of the RSM (all impact values: 3.0; all sensitivities: medium)

| Response variable | Unit | Analysis | Goal | Target |
|---|---|---|---|---|
| **Degree of curing** | - | Mean | Maximize | - |
| **Width** | mm | Mean | Hit target | 0.5 |
| **Height** | mm | Mean | Hit target | 0.2 |
| **Length** | mm | Mean | Hit target | 50.0 |

In the next step, the process parameters PS and EM were defined as input variables of the RSM. EM scaled the commanded material delivery, whereas PS determined the relative movement between the nozzle and the deposited material and thereby influenced both material distribution and the time available for local UV-induced shape stabilization. Low and high factorial levels were defined for the input variables according to the findings of the preliminary studies. The values are listed in Table 4. The water content of the hydrogel formulation was set to the non-continuous values of 10 wt% ($HG_{hwc}$) and 7.5 wt% ($HG_{lwc}$).

**Table 4** Experimental input variables of the RSM to be varied (all types: continuous; all roles: controllable)

| Input variable | Unit | Low factorial level | High factorial level |
|---|---|---|---|
| **Printing speed** | mm $s^{-1}$ | 1.5 | 5.0 |
| **Extrusion multiplier** | - | 0.8 | 2.3 |

Subsequently, a rotatable central composite design with two factors was utilized to generate a total of twelve design points for each hydrogel formulation [29], [30]. These design points include four factorial points, four center points, and four axial star points that extend the investigated

parameter range to PS = 0.78–5.73 mm $s^{-1}$ and EM = 0.49–2.61. The full experimental design is uploaded in the SDS of this paper [28].

Each design point was 3D-printed three times with both selected hydrogel formulations leading to a total of 72 printed tracks. The UV ringlight was only turned on while the precursor extruder was active. Samples were labeled $HG_x$-y.z, where x denotes the hydrogel formulation (hwc or lwc), y denotes the parameter combination within the DoE (1–12), and z denotes the individual replicate (1–3). The tracks were photopolymerized in situ without additional post-print UV exposure.

The geometric characteristics of the hydrogel precursor tracks were determined using a VR Series ONE-SHOT 3D measurement microscope from Keyence Corporation (Osaka, Japan). High-resolution surface topographies were generated and analyzed using the integrated software. Track width and height were evaluated at three predefined positions per track, with each value averaged over a 5 mm measurement interval. The three positional values were then averaged to obtain one width and height value per track. Track length was measured once per track using automated edge detection. For each design point, mean values and standard deviations were calculated across the three replicate tracks. The response surface models were fitted to these mean response values of the twelve design points, each based on three replicate tracks. Because of the low optical reflectivity and translucency of the hydrogel precursors, the specimens were coated with the fine-grained scanning spray 3D Laserscanning Entspiegelungsspray from Helling (Heidgraben, Germany) before height measurement.

The printing behavior of the hydrogel formulations was evaluated based on deviations from the specified geometric targets, dimensional consistency, degree of curing, and printability. The degree of curing was evaluated qualitatively using a three-level ordinal scale. A score of 1 indicated insufficient curing, with inadequate structural integrity preventing damage-free removal from the build plate. A score of 2 indicated sufficient curing: the specimens were dimensionally stable and removable using a spatula, although minor residues remained and additional UV exposure caused pronounced visual changes. A score of 3 indicated a high degree of curing, characterized by straightforward removal without residue and negligible visual changes upon further UV exposure. A print was classified as successful when a continuous track with a curing score of at least 2 was obtained. Systematic deviations from the target dimensions were evaluated separately as quantitative responses of the DoE and were therefore not considered printing failures.

The response data were analyzed using main-effect plots and Pareto charts of standardized effects. Statistical significance was assessed at $p < 0.05$, corresponding to a critical standardized effect of approximately 2.45 in the Pareto charts based on six residual degrees of freedom. A numerical process-parameter optimization was subsequently carried out for the selected hydrogel formulation using the response surface models for track width and height. Track length and degree of curing were excluded because their models showed insufficient predictive capability. The resulting parameter combination was then validated experimentally using the same manufacturing and characterization procedures.

#### 3.2.4. Shrinkage Behavior

The shrinkage behavior of the hydrogel formulation $HG_{hwc}$ was characterized by determining the percentage mass-based shrinkage of hydrogel monoliths. Three batches of freshly prepared hydrogel precursor with identical compositions ($HG_{hwc}(1)$, $HG_{hwc}(2)$, $HG_{hwc}(3)$) were used to manufacture three 3 mm × 3 mm × 30 mm sized monoliths from each batch (nine samples in total) by casting the precursor into a 3D-printed polymer mold followed by manual UV-induced

photopolymerization until no further color change was visible. The masses and weight percentages of all precursor constituents used in this experiment can be found in the SDS of this paper [28]. The initial mass of all samples was measured after fabrication, followed by a 24 h initial swelling step in sealed, water-filled containers immersed in a 25 °C water bath. Subsequently, the swollen monoliths were weighed and transferred into the same water bath for 24 h, this time at 40 °C for thermal shrinkage. Before weighing, the samples were patted dry. The temperature-induced mass-based shrinkage was then evaluated by determining the percentage mass loss between the swollen state at 25 °C and the thermally contracted state at 40 °C. Additionally, the mean value was determined from all individual measurements.

### 3.2.5. Shrinkage Kinetics

The shrinkage kinetics of the hydrogel formulation $HG_{hwc}$ were investigated using an image-based measurement setup, according to the procedure described by Eckert et al. [31]. Three hydrogel monoliths measuring 5 mm × 5 mm × 30 mm containing an integrated cannula were fabricated using a new additively manufactured mold and manual UV-induced photopolymerization as described in 3.2.4. The enlarged specimen dimensions were used for improved contour detection and to facilitate the integration of the cannula. They were suspended in a temperature-controlled water bath inside a light-shielded Duclus DU5041 imaging box. The experimental procedure used the same three precursor batches ($HG_{hwc}(1)$, $HG_{hwc}(2)$, $HG_{hwc}(3)$) and followed the same temperature protocol as described for the shrinkage behavior in subsection 3.2.4. As shown in Fig. 2, a C1 Pro camera from Kurokesu (Vilnius, Lithuania) positioned in front of the water bath automatically acquired images every 30 s throughout the experiment using a custom acquisition program. The recorded images were preprocessed in the Fiji distribution of the open-source software ImageJ (version 1.54p) by cropping the region of interest, converting the images to grayscale, and applying an intensity threshold to obtain binary images (shown in Fig. 2b). The recorded image sequences were then analyzed using a Python script based on OpenCV image processing. The script was originally developed by Eckert et al. [31] and subsequently adapted and extended for the specific requirements of the present study [28]. The hydrogel area was extracted by grayscale thresholding, and the shrinkage kinetics were determined by calculating the normalized volume ($V/V_0$) of the monoliths over time. $V_0$ represents the equilibrium specimen volume at 25 °C. For practical reasons, however, $V_0$ was determined from the first image acquired immediately after transferring the specimen to 40 °C, before any measurable temperature-induced shrinkage occurred. Assuming a square cross-section of the monoliths, the width measured from the images was considered equal to the depth. The volume was calculated from the resulting cross-sectional area and the measured monolith length.

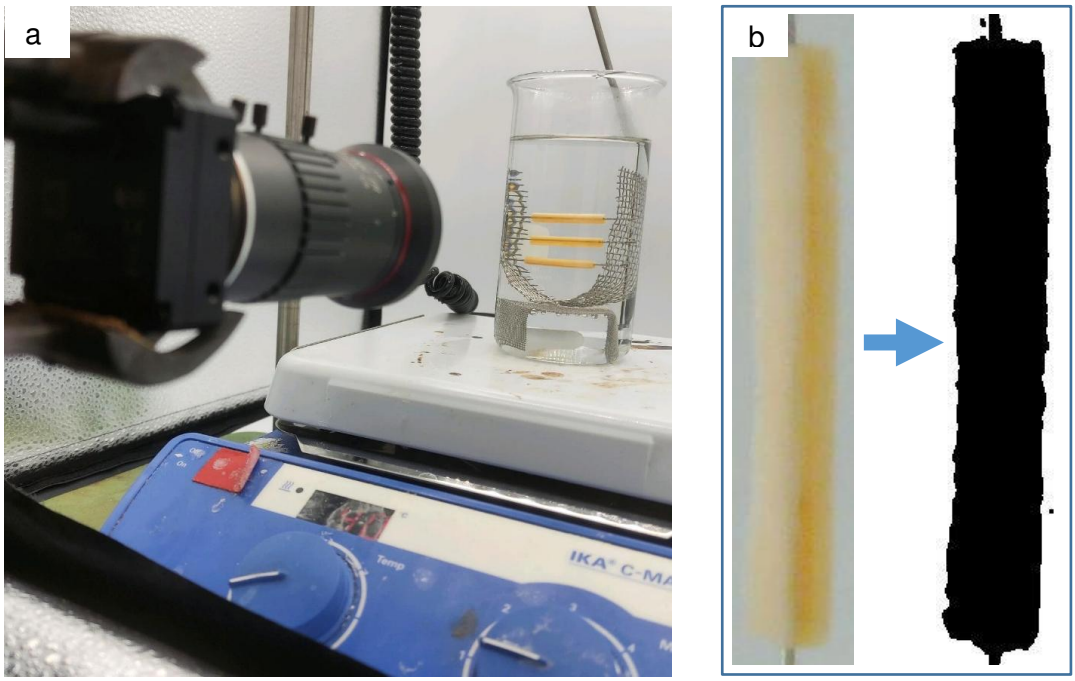



**Fig. 2** Camera setup for image-based hydrogel shrinkage kinetics measurements (a), exemplary image editing of shrinkage kinetics sample by applying intensity threshold (b)

### 3.2.6. Shrinkage-induced Bending of Multi-material Plates

The objective of this investigation was to evaluate whether the contraction force of the hydrogel was sufficient to induce bending of polymer components and whether the interfacial adhesion between both materials was adequate to transmit the resulting mechanical loads. The hydrogel precursor batch $HG_{hwc}(1)$, introduced in subsection 3.2.4, was selected for this examination. For this purpose, six nominally identical multi-material bilayer test specimens, intended to account for specimen-to-specimen variability and assess experimental reproducibility, were additively manufactured using the developed printer setup. Each specimen consisted of a TPU base plate measuring 0.4 mm × 15 mm × 60 mm with a 0.8 mm thick hydrogel precursor layer printed on top. The printing process is shown in Fig. 3. The resulting multi-material specimens were subjected to the same swelling and shrinkage protocol described for the hydrogel monoliths in subsection 3.2.4. During the initial experiment, however, the hydrogel detached completely from the TPU substrates upon shrinking, preventing any meaningful assessment of the bending behavior. This experiment therefore demonstrated that the interfacial adhesion between the printed hydrogel and the smooth TPU surface was insufficient to withstand the shrinking-induced stresses. To improve the mechanical interlocking between both materials, the TPU base plates were modified by incorporating nine small bridge-like structures and twelve through-holes, allowing the precursor to anchor mechanically to the polymer substrate after polymerization. Fig. 10a shows the printed bilayer samples and Fig. 10e the CAD file of the modified TPU base plate. The experiment was subsequently repeated using the modified specimen geometry following the same experimental procedure as described previously.

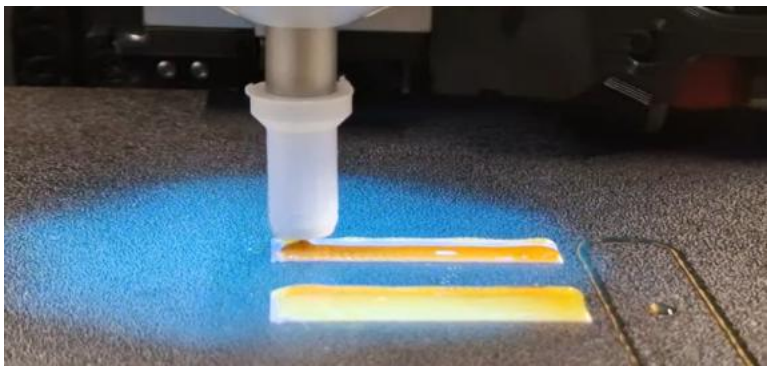


**Fig. 3** Fabrication of hydrogel-TPU bilayer specimens for shrinkage-induced bending experiments. The white TPU base plate (60 mm in length) is shown for scale

The bending of the multi-material bilayer specimens was quantified by image-based curvature analysis. Photographs of both longitudinal side faces were acquired from each specimen in the initially swollen and fully shrunken states with the camera oriented perpendicular to the respective side face. The images were processed in Fiji, where the pixel size (pixels/mm) was calibrated using a reference ruler positioned in every image. The specimen centerline was traced using the spline tool, interpolated, and exported as coordinate data. The coordinates were then analyzed in the software MATLAB from MathWorks (Natick, USA) using a custom script, which performed a linear least-squares circle fit to determine the radius (r) of curvature (κ). The curvature magnitude was calculated from the fitted circle as $|\kappa| = 1/r$. Signs were assigned according to the bending direction relative to a fixed specimen coordinate convention. Under this convention, the swollen states exhibited negative and the shrunken states positive curvature.

The normalized root-mean-square error (RMSE/r) of the radial residuals was used as a dimensionless indicator of the circle-fit quality. Curvature values from both specimen sides were averaged separately for each state, and bending was quantified as the change in mean signed curvature, $\Delta\kappa = \kappa_{shrunk} - \kappa_{swollen}$, between the swollen (25 °C) and shrunken (40 °C) states.

## 4. Results and Discussion

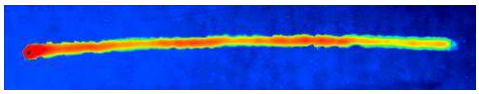
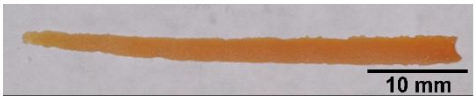
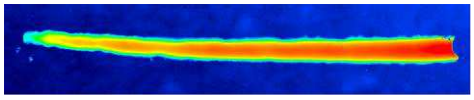
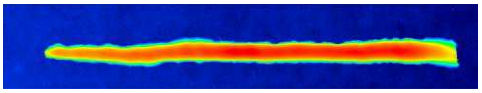
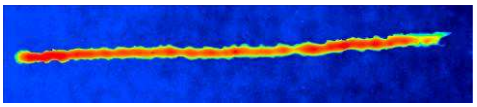
In this section, the results of this work are presented and discussed. For more detailed information on specific values and the analysis done in this work, the reader is kindly referred to the SDS [28], containing relevant results, additional pictures and plots, used software codes, and information about the hydrogel formulations.

### 4.1. Hydrogel Design of Experiments

#### 4.1.1. Qualitative Deposition Phenomena

Four characteristic local deposition phenomena were observed that were not modeled as separate DoE responses and are therefore only partly reflected in the mean dimensions and standard deviations: transient material accumulation, progressive track enlargement, end-of-track deformation, and periodic width modulation. Table 5 presents representative photographs and 3D-scanned surface-height maps of these phenomena. These qualitative observations complement the quantitative DoE analysis by illustrating local and transient process behavior that cannot be adequately described by mean geometric values alone.

**Table 5** Representative photographs and 3D-scanned surface-height maps of selected tracks illustrating characteristic deposition phenomena. 3D-scanned surface-height maps are presented only qualitatively and the elevation legends are scaled differently for every picture. The printing direction is from left to right

| | Exemplary sample | |
|---|---|---|
| **Phenomenon** | **Photograph** | **3D-scanned surface-height maps** |
| **Transient material accumulation ($HG_{lwc}$-12.3)** |   |  |
| **Progressive track enlargement ($HG_{hwc}$-10.2)** |   |  |
| **End-of-track deformation ($HG_{lwc}$-7.3)** |   |  |
| **Periodic width modulation ($HG_{lwc}$-12.1)** |   |  |

Localized increases in track width or height were observed at the beginning of several tracks. Sample $HG_{lwc}$-12.3 in Table 5 illustrates this transient material accumulation. The feature suggests that steady-state material discharge was not necessarily established when the printing movement began. Material accumulated at the nozzle before printing, as illustrated in Fig. 4, and transient discharge during the onset of extrusion may both contribute to the increased local material volume. Formulation-dependent flow behavior may represent an additional factor because rheological properties can affect the sensitivity of hydrogel formulations to extrusion parameters [32]. However, because the rheological properties of $HG_{hwc}$ and $HG_{lwc}$ were not characterized, their contribution cannot be determined from the present measurements.

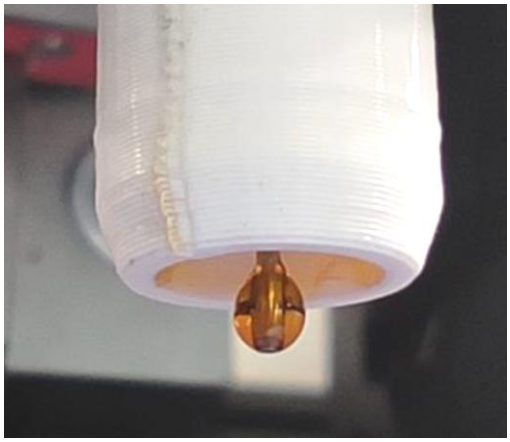


**Fig. 4** Hydrogel precursor accumulation at the nozzle tip. The surrounding shadow-casting shield is made of white PLA

A second characteristic phenomenon is the progressive track enlargement along the printing direction. Sample $HG_{hwc}$-10.2 in Table 5 shows a continuous increase in both width and height from the beginning toward the end of the track. Because PS and EM remained constant within the track, these parameters alone cannot explain the progressive dimensional change. The

simultaneous increase in width and height indicates an increasing local cross-sectional area and therefore suggests a transient increase in the actual amount of material deposited per unit length. Insufficient shape stabilization may additionally allow the material to flow and spread after deposition. However, spreading alone cannot explain the concurrent increase in height. Extrudate swell may further affect the local dimensions of viscoelastic hydrogel formulations [33], although it does not independently explain the progressive change along the printing path. The relative contributions of transient material discharge, rheological behavior, and curing kinetics cannot be distinguished using the present measurements.

A third phenomenon is a local increase in track width accompanied by a reduction in height near the end of deposition, as illustrated by sample $HG_{lwc}$-7.3 in Table 5. Qualitative inspection suggested that this end-of-track deformation was more apparent at high EM settings. After the commanded end of extrusion, residual pressure or elastic energy within the extrusion system may cause continued material discharge and increase the local material volume [34]. At high EM settings, the larger deposited volume may require a greater UV dose for sufficient shape stabilization. Because the printhead and UV source move away immediately after the deposition ends, the material may not receive a sufficient UV dose before irradiation decreases. The resulting increase in width and reduction in height is consistent with lateral spreading and partial collapse of insufficiently shape-stabilized material. Comparable behavior has been reported for extrusion-printed materials with insufficient shape retention, whereas in situ UV irradiation can reduce spreading and sagging during deposition [35], [36].

The fourth characteristic phenomenon consists of small, periodic reductions in track width along the printing direction. Sample $HG_{lwc}$-12.1 illustrates this periodic width modulation in Table 5. Qualitative inspection suggested that these modulations occurred in both formulations and were more apparent at lower EM settings. At lower material delivery, the smaller deposited volume may cover the structured build plate less effectively, increasing the relative influence of its topography on the first-layer geometry. The insufficiently stabilized hydrogel precursor may locally conform to the surface structure and become pinned during UV-induced stabilization, producing periodic constrictions along the track. However, because neither the build plate topography nor its spatial correspondence with the track modulations was investigated, this mechanism remains hypothetical. The observation therefore suggests a potential practical limitation when reducing EM but does not establish a universal lower EM boundary for both formulations. The influence of build plate topography should therefore be investigated systematically in future studies.

Together, these phenomena reveal local sources of geometric variation that were not modeled as separate DoE responses. Transient material discharge, uncharacterized rheological behavior, UV-induced shape stabilization, and substrate interactions may contribute to the observed features, but their individual effects cannot be resolved using the present post-print measurements.

### 4.1.2. Effects of Process Parameters

To quantitatively assess the systematic influence of the process parameters PS and EM on track geometry and degree of curing, the standardized Pareto charts [28] and main-effect plots (shown in Fig. 5) of the DoE are evaluated in the following. In the response surface model, A denotes PS, B denotes EM, AA and BB represent their respective quadratic effects, and AB represents their interaction. The observed trends were generally consistent with the expected process behavior, with increasing PS resulting in shorter tracks and increasing EM generally increasing track width and height, whereas its effect on track length remained comparatively small and statistically

nonsignificant. Overall, the measured track lengths remained below the target value, whereas track widths and heights consistently exceeded their respective targets, indicating that the specified dimensions could not be fully achieved within the specified factor bounds.

PS is the only statistically significant process parameter affecting track length for both formulations, with standardized effects of 3.4 ($HG_{hwc}$) and 2.9 ($HG_{lwc}$), exceeding the significance threshold of 2.45 ($p < 0.05$). As shown in the main-effect plot a) of Fig. 5, both formulations show a comparable decrease in track length up to approximately 3.5 mm $s^{-1}$, above which $HG_{hwc}$ decreases more strongly. This may indicate the onset of an unfavorable deposition regime for the presumably lower-viscosity $HG_{hwc}$, where continuous track deposition has not yet been established and increased material retention at the nozzle shifts the effective start and end positions of the track. The magnitude of the EM effect is larger for $HG_{lwc}$ than for $HG_{hwc}$, but it does not reach the significance threshold for either formulation, which is consistent with the comparatively shallow and slightly curved main-effect profiles. Similarly, the PS-EM interaction term (AB) and quadratic terms (AA, BB) remain below the threshold, indicating that neither EM, interactions, nor quadratic effects significantly influence track length within the investigated parameter range. Nevertheless, slight and oppositely directed curvatures are observed for PS and EM. As neither quadratic nor interaction terms are statistically significant, this behavior cannot be attributed to a systematic effect based on the present data. Instead, it may partly arise from stochastic process variations not captured by the model, such as fluctuations in nozzle pressure, temporary partial blockages, air inclusions, or material accumulation at the nozzle.

EM shows the strongest standardized effect on track height for both formulations, particularly for $HG_{lwc}$, with standardized effects of approximately 5.5 for $HG_{hwc}$ and 14.8 for $HG_{lwc}$, clearly exceeding the significance threshold. PS remains below the threshold for $HG_{hwc}$, whereas it slightly exceeds the threshold for $HG_{lwc}$. As shown in the main-effect plot b) of Fig. 5, increasing PS generally reduces track height, while increasing EM produces a pronounced and approximately linear increase in height for both formulations; the latter is supported by the small and nonsignificant quadratic BB terms. Among all evaluated main-effect responses, the largest formulation-dependent difference is observed in the PS response for track height with $HG_{lwc}$ producing higher tracks along the investigated PS range. $HG_{hwc}$ exhibits a distinct curvature with a slight initial increase followed by a pronounced decrease starting at approximately PS = 2.6 mm $s^{-1}$. In contrast, $HG_{lwc}$ shows a moderate and continuous decrease over the examined range. The more pronounced variation in the $HG_{hwc}$ main-effect profile may reflect a greater susceptibility of the $HG_{hwc}$ formulation to changes in deposition conditions. Its higher water content and the presumably associated reduction in viscosity may facilitate flow and deformation of the deposited precursor before sufficient curing is achieved, thereby promoting a greater reduction in track height. A larger change in track height across the EM range is observed for $HG_{hwc}$, although the standardized EM effect is substantially stronger for $HG_{lwc}$. This likely results from differences in residual variability and coefficient uncertainty between the two models. The interaction term AB and the quadratic terms AA and BB remain below the significance threshold, indicating that the observed trends are primarily governed by the linear effects of PS and EM.

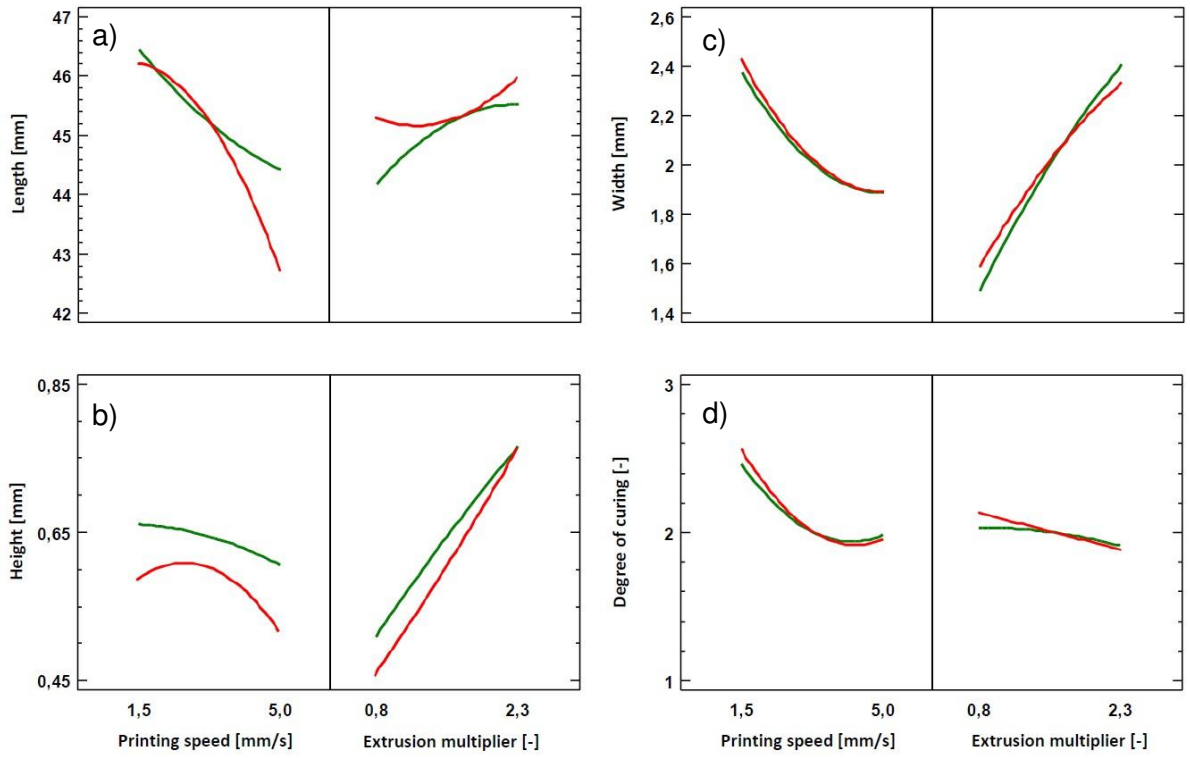



**Fig. 5** Main-effects of PS and EM on track length (a), height (b), width (c), and degree of curing (d) for the hydrogel formulations $HG_{hwc}$ (red lines) and $HG_{lwc}$ (green lines). The lines represent second-order response surface model predictions rather than experimental data points, with their curvature resulting from the quadratic model terms

Both PS and EM are identified as statistically significant process parameters affecting track width for both formulations, with EM showing the strongest influence (standardized effects of approximately 9.0 for $HG_{hwc}$ and 8.1 for $HG_{lwc}$), followed by PS (approximately 6.3 and 4.3, respectively). As shown in the main-effect plot c) of Fig. 5, increasing PS results in decreasing track width, whereas increasing EM produces wider tracks. These trends may result from changes in extrusion dynamics, precursor spreading, and local UV exposure time as PS increases, whereas higher EM increases the commanded material deposition. The PS response shows a slightly more pronounced curvature for $HG_{hwc}$ than for $HG_{lwc}$, which is reflected by the significant quadratic PS term AA for $HG_{hwc}$, while the corresponding term for $HG_{lwc}$ remains just below the significance threshold. In contrast, the EM response is approximately linear for both formulations, as the quadratic term BB remains insignificant. The PS-EM interaction AB also remains below the significance threshold, indicating no statistically significant interaction between PS and EM within the investigated parameter range.

Because the curing score is ordinal but was treated numerically by the response surface model, the following results are interpreted as exploratory. PS exhibits the strongest influence on the degree of curing for both formulations, as demonstrated by the main-effect plot d) of Fig. 5 and the standardized effects of approximately 5.5 for $HG_{hwc}$ and 4.1 for $HG_{lwc}$. Increasing PS initially causes a pronounced reduction in the degree of curing, followed by a slight recovery at the highest speeds. This nonlinear response is supported by the significant AA terms for both formulations and may result from two competing mechanisms: higher speeds reduce the local UV exposure time, while speed-dependent changes in actual extrusion and track geometry might additionally alter light penetration. For $HG_{hwc}$, a significant AB interaction is additionally observed, suggesting that the effect of PS varies with EM, potentially reflecting the combined influence of deposition rate and local UV exposure on the degree of curing. The corresponding AB term is not statistically significant for $HG_{lwc}$. Compared with the other investigated responses, EM produces the smallest

changes in the main-effect plots for degree of curing and does not constitute a significant individual factor for either formulation. For $HG_{hwc}$, the degree of curing decreases nearly linearly with increasing EM. However, the effect does not reach statistical significance. The small and nonsignificant BB terms further suggest that no relevant nonlinear dependence on EM occurs within the investigated range.

### 4.1.3. Model Evaluation and Parameter Optimization

Model quality is evaluated using the adjusted coefficient of determination ($R^2_{adj}$) and the predicted coefficient of determination ($R^2_{pred}$). The conventional $R^2$ describes the proportion of observed response variability explained by the fitted model but is not used as a primary evaluation criterion because it does not account for model complexity. $R^2_{adj}$ is therefore used to evaluate model fit while accounting for the number of model terms, whereas $R^2_{pred}$ provides an estimate of the model's predictive capability.

The degree of curing is assessed on an ordinal scale and therefore does not represent a continuous quantitative response. Additionally, it shows limited predictive performance, with an $R^2_{adj}$ of 83.89% but an $R^2_{pred}$ of only 37.52%. Consequently, the degree of curing is excluded from the subsequent numerical optimization. Track length is disregarded because its adjusted and predicted $R^2$ values of 54.47% and 2.32%, respectively, indicate insufficient model performance for reliable optimization. The limited predictability of track length is consistent with the observed sensitivity to stochastic start- and end-of-track effects that are not represented by PS and EM. $HG_{lwc}$ is excluded from the final optimization primarily because of its insufficient formulation stability, including the formation of visible crystallized threads shortly after preparation (shown in [28]). Additionally, $HG_{lwc}$-8 (PS = 0.78 mm $s^{-1}$; EM = 1.55) is the only parameter combination that could not be printed reliably and reproducibly. Except for track height, the $HG_{lwc}$ models also show lower adjusted and predicted $R^2$ values than those of $HG_{hwc}$. Based on these considerations, the numerical parameter optimization is restricted to track width and height of $HG_{hwc}$ and the $HG_{hwc}$ formulation is also chosen for all further investigations of this paper. For $HG_{hwc}$, the width model shows high adjusted and predicted $R^2$ values of 92.14% and 86.35%, respectively, indicating strong model fit and comparatively high predictive performance. The height model reaches an $R^2_{adj}$ of 73.43% but a considerably lower $R^2_{pred}$ of 37.49%, indicating substantially greater uncertainty in its predictive capability. The final numerical optimization of the $HG_{hwc}$ width and height models identified PS = 5.27 mm $s^{-1}$ and EM = 0.66 as the model-derived parameter combination within the investigated process window.

### 4.1.4. Experimental Validation

Three hydrogel precursor tracks were printed to validate the optimized parameter set. The samples were characterized using the same measurement procedure as in the DoE, allowing direct comparison with the model predictions. The averaged results of this validation are listed together with the predicted values, and the percentage deviations between predicted and measured values in Table 6.

**Table 6** Predicted and mean measured response variable values of the optimized parameter set

| Response variable | Predicted value | Measured value | Deviation from prediction |
|---|---|---|---|
| **Length** | 40.46 mm | 47.30 ± 0.37 mm | + 16.91% |
| **Height** | 0.37 mm | 0.43 ± 0.01 mm | + 16.22% |
| **Width** | 1.40 mm | 1.50 ± 0.02 mm | + 7.14% |
| **Degree of curing** | 1.79 | 2 ± 0.00 | + 0.21 score units |

The experimental validation reveals differences between the predicted and measured responses of the model-derived parameter combination. The measured track width and height exceed the predicted values by 7.14% and 16.22%, respectively. However, both dimensions remain substantially above their specified targets: the measured width of 1.50 ± 0.02 mm exceeds the 0.50 mm target by 200%, and the measured height of 0.43 ± 0.01 mm exceeds the 0.20 mm target by 115%. The measured track length of 47.30 ± 0.37 mm exceeds the predicted value by 16.91% but remains 5.40% below the target of 50 mm. The observed curing score of 2 ± 0.00 indicates sufficient curing and is higher than the predicted value of 1.79, with the non-integer prediction resulting from the numerical treatment of the ordinal response by the regression model. Although track width exhibits the smallest deviation from its model prediction, consistent with the highest $R^2_{pred}$ among all $HG_{hwc}$ responses, it also shows the largest deviation from the intended geometric target.

Although DoE parameter set $HG_{hwc}$-12 (PS = 3.25 mm $s^{-1}$; EM = 0.49) produces track widths and heights (1.43 ± 0.02 mm and 0.37 ± 0.02 mm) closer to the target dimensions, the model-derived parameter combination offers several advantages regarding process reliability and geometric consistency. Its mean track length of 47.30 ± 0.37 mm slightly exceeds the 46.47 ± 0.82 mm achieved with parameter set 12 and is accompanied by a considerably lower standard deviation. The standard deviation in track height is also reduced, indicating more uniform deposition. The standard deviation in track width is ± 0.02 mm for both parameter sets. Moreover, all three validation tracks were printed successfully on the first attempt, whereas one of the three samples produced with parameter set 12 required two additional attempts. These results suggest that the optimized settings provide a favorable balance between dimensional consistency, track length, and process reliability, despite not achieving the specified width and height targets. Furthermore, the comparison with parameter set $HG_{hwc}$-12 highlights the trade-off between dimensional accuracy and process robustness within the investigated parameter range.

## 4.2. Shrinkage Behavior

The thermoresponsive behavior of $HG_{hwc}$ is evaluated by determining the mass-based shrinkage of hydrogel monoliths during the transition from the swollen state at 25 °C to the shrunken state at 40 °C. Prior to the temperature-induced shrinkage, free swelling at 25 °C results in an initial averaged mass increase of 13.14 ± 4.28% relative to the as-built state. Subsequently, the three independently prepared hydrogel precursor batches exhibit shrinkages of 57.19 ± 2.04%, 54.55 ± 2.87%, and 50.92 ± 1.73% relative to the swollen state, respectively, resulting in an overall average of 54.22 ± 3.36% during the transition from 25 °C to 40 °C. These results are

presented in a bar chart in Fig. 6. The mean shrinkage decreases from $HG_{hwc}(1)$ to $HG_{hwc}(3)$, while the relatively small standard deviations within each batch indicate consistent behavior among the respective monoliths. The differences between batches suggest that minor variations during precursor preparation may influence the magnitude of the response, although substantial mass loss is observed for all three batches. Overall, these results demonstrate a substantial and reproducible thermoresponsive behavior of the $HG_{hwc}$ hydrogel formulation across independently prepared batches.

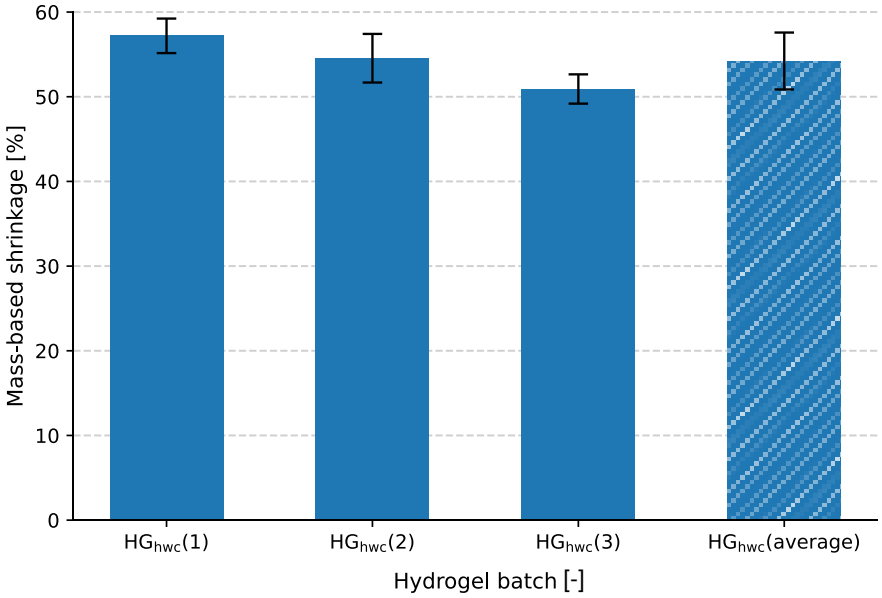



**Fig. 6** Mean mass-based shrinkage and standard deviation for individual $HG_{hwc}$ batches from three samples each and average of all nine samples

### 4.3. Shrinkage Kinetics

The temperature-induced shrinkage kinetics of the three $HG_{hwc}$ batches are shown in Fig. 7 as mean normalized volume over time including the standard deviation as error range. Short-term fluctuations are visible in the data, particularly after the initial contraction. These fluctuations are attributed primarily to limitations of the image-based measurement method, including small movements or rotations of the suspended monoliths and variations in the contour detection during thresholding.

Although images are acquired throughout the 24 h shrinkage phase, evaluation of the complete sequences confirms that the relevant volume changes occur within the first 30 min. Most contraction takes place within the first 5–10 min, and an apparent volumetric plateau was reached after approximately 16–18 min. At 30 min, $V/V_0$ is approximately 0.67, 0.70, and 0.71 for $HG_{hwc}(1)$, $HG_{hwc}(2)$, and $HG_{hwc}(3)$, respectively, corresponding to volumetric reductions of 33%, 30%, and 29%. Thus, $HG_{hwc}(1)$ exhibits the greatest shrinkage, followed by $HG_{hwc}(2)$ and $HG_{hwc}(3)$. This batch-dependent order agrees with the one obtained from the mass-based shrinkage measurements of subsection 4.2, supporting consistency of the observed batch-dependent trend across both measurement approaches. The mean normalized volume after 30 min is approximately $0.69 \pm 0.02$ (31% volumetric reduction).

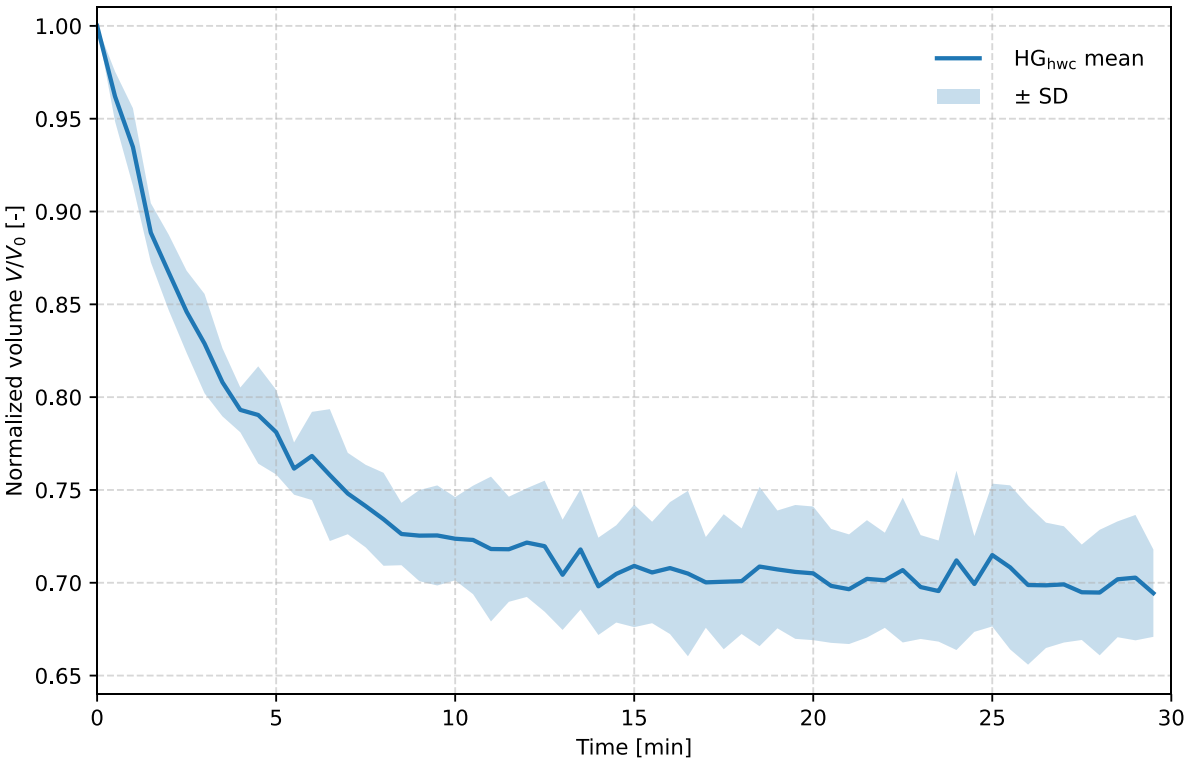



**Fig. 7** Mean normalized volume $V/V_0$ over time of three $HG_{hwc}$ hydrogel precursor samples at 40 °C, each fabricated from an independently prepared batch of the same formulation. The mean is shown as solid blue line and ± standard deviation as shaded area

The mass-based and volume-based shrinkage values differ considerably between the methods. However, the gravimetric method quantifies mass loss, whereas the image-based method estimates volume from a two-dimensional projection. The different measurement approaches, deviations from the assumed square cross-section, differently sized monoliths, and segmentation uncertainties during image thresholding may therefore contribute to the observed differences, preventing a direct quantitative comparison between the two measures. Furthermore, the presence of parts of the cannula in the analyzed images (Fig. 2b) presumably introduces a systematic bias into the measurement results. Consequently, the kinetic measurements are primarily used to characterize the rate and temporal progression of the shrinking process, while the gravimetric measurements provide the more direct quantitative measure of mass-based shrinkage.

### 4.4. Shrinkage-induced Bending of Multi-material Plates

The curvature analysis demonstrates a clear temperature-induced bending response for all six multi-material specimens. Because the specimens bend in opposite directions in the swollen and shrunken states, curvature κ is evaluated as a signed quantity according to the coordinate convention defined in subsection 3.2.6. Under this convention, the swollen states ($\kappa_{swollen}$) exhibit negative and the shrunken states ($\kappa_{shrunk}$) positive curvatures. Accordingly, the curvature change is calculated as $\Delta\kappa = \kappa_{shrunk} - \kappa_{swollen}$ and visualized as a bar chart in Fig. 8.

The individual curvature changes range from 0.0343 to 0.0550 $mm^{-1}$, with samples 2 and 3 exhibiting the smallest changes of $0.0344 \pm 0.0012$ and $0.0343 \pm 0.0003$ $mm^{-1}$, respectively. Overall, a complete reversal in bending direction for every specimen is demonstrated with an average curvature change of $0.0444 \pm 0.0084$ $mm^{-1}$. This behavior is illustrated in Fig. 10b and c

for sample 6 in the swollen and shrunken states, respectively. Fig. 10a additionally shows all specimens directly after printing, before any meaningful bending occurs.

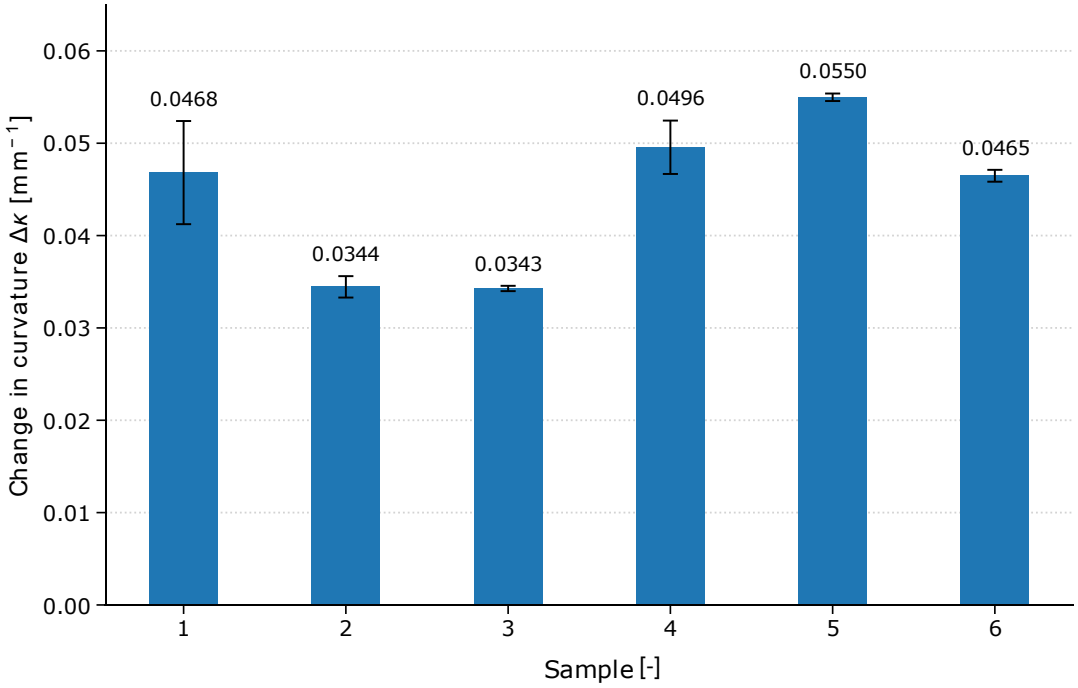



**Fig. 8** Change in signed curvature Δκ for each hydrogel-TPU bilayer specimen. Error bars represent the sample standard deviation of two paired curvature changes per specimen, calculated separately for the two longitudinal side views (n = 2)

Fig. 9 shows the signed curvatures of each sample in the swollen and shrunken states. The dotted horizontal line represents the as-built state with no curvature. In the swollen state, the signed curvatures are comparatively similar, ranging from −0.0247 to −0.0179 $mm^{-1}$ (average: −0.0218 ± 0.0024). At this stage, no cracking of the hydrogel layer is observed, and the specimens exhibit comparatively uniform bending. In contrast, substantially greater differences appear in the shrunken state, where curvature ranges from 0.0123 to 0.0320 $mm^{-1}$ (average: 0.0226 ± 0.0079). Consequently, the variation in Δκ is primarily attributed to differences in the shrunken-state curvature rather than the initial swollen-state geometry.

This is consistent with the observed crack formation: Samples 2 and 3, which exhibit the most pronounced cracking, also show the lowest shrunken-state curvatures of 0.0140 ± 0.0001 and 0.0123 ± 0.0026 $mm^{-1}$, respectively, and consequently the smallest curvature changes Δκ. In contrast, specimens with less pronounced cracking retain a larger continuous hydrogel area for transferring contraction into bending and reach higher shrunken-state curvatures. This relationship suggests that pronounced cracking may reduce the effective transfer of hydrogel contraction into macroscopic bending, although additional specimen-specific variations cannot be excluded. The differences in crack formation are illustrated in Fig. 10, showing sample 3 in panel d) as an example of pronounced crack formation and sample 6 in panel c) as an example with comparatively fewer cracks. The corresponding variations in the shrunken-state curvature are consistent with the extent of hydrogel damage observed in the specimens.

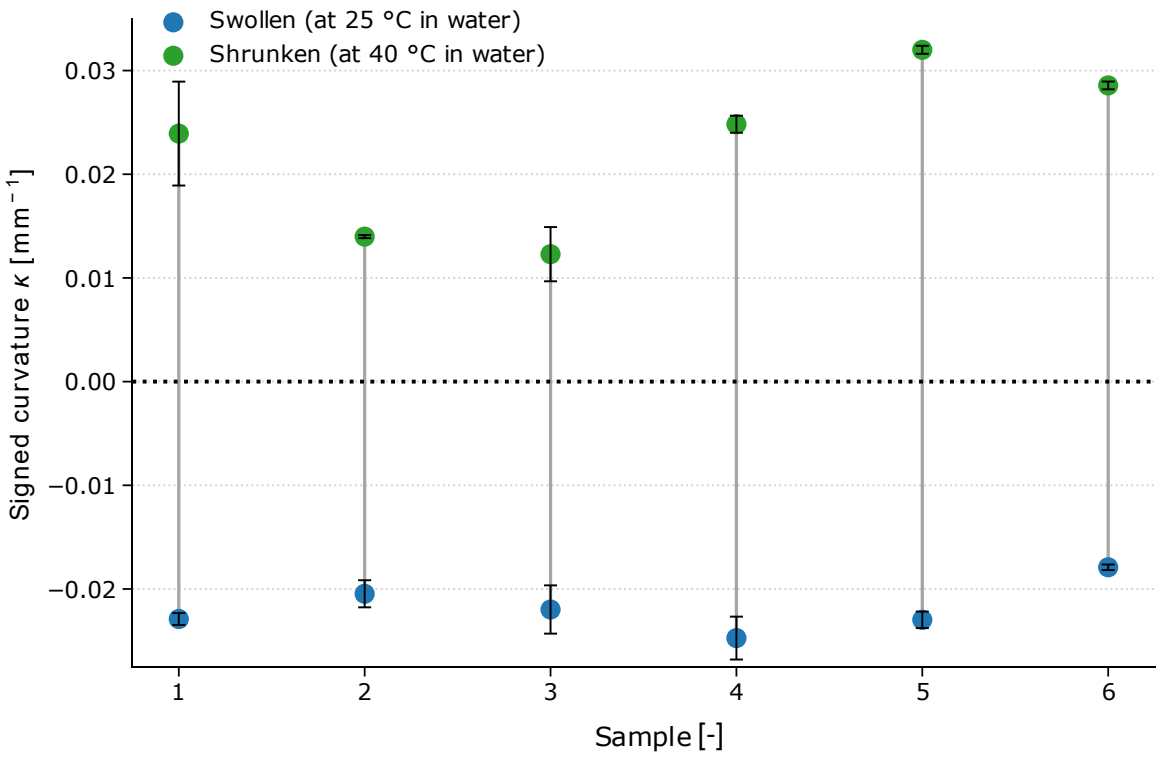



**Fig. 9** Signed curvature κ of each hydrogel-TPU bilayer specimen in the swollen and shrunken states. Error bars represent the sample standard deviation between the two longitudinal side views for each specimen and hydrogel state (n = 2)

RMSE/r provides a dimensionless measure of the specimen's deviation from an ideal circular arc. In the swollen state, RMSE/r remains consistently low, between $1.07 \times 10^{-3}$ and $2.79 \times 10^{-3}$, whereas values increase after shrinkage for every specimen to between $3.54 \times 10^{-3}$ and $12.51 \times 10^{-3}$. The systematically increased fitting errors in the shrunken state indicate greater deviations from an ideal circular arc. This increased geometric irregularity coincides with the formation of cracks during shrinkage, although other effects, such as locally nonuniform contraction and measurement uncertainties, may also contribute to the increased RMSE/r.

The fact that cracks occur exclusively during shrinkage at 40 °C and only after the modification of the TPU substrate may be attributed to the altered mechanical constraint at the hydrogel-TPU interface. In the original design, the hydrogel delaminates from the TPU, allowing interfacial separation to release stresses generated by the deformation mismatch. The bridges and holes of the modified substrate reduce or prevent complete delamination through mechanical interlocking. During swelling, the constrained hydrogel primarily generates compressive stresses along the interface, which can be accommodated by bending and out-of-plane deformation. During shrinkage, however, the hydrogel tends to contract while remaining anchored to the comparatively dimensionally stable TPU substrate, producing tensile and shear stresses within the hydrogel layer. These stresses are further concentrated around the discrete anchoring features and may locally exceed the fracture resistance of the hydrogel. Local variations in the degree of curing within the hydrogel layer, potentially introduced by shadowing from the bridges may further contribute to the observed differences in crack formation. The modification therefore appears to shift the dominant failure mechanism from interfacial delamination to cohesive cracking within the hydrogel. Despite this partial failure, all specimens exhibit substantial curvature reversal, confirming that the mechanically interlocked configuration successfully transfers the thermoresponsive deformation into macroscopic bending.

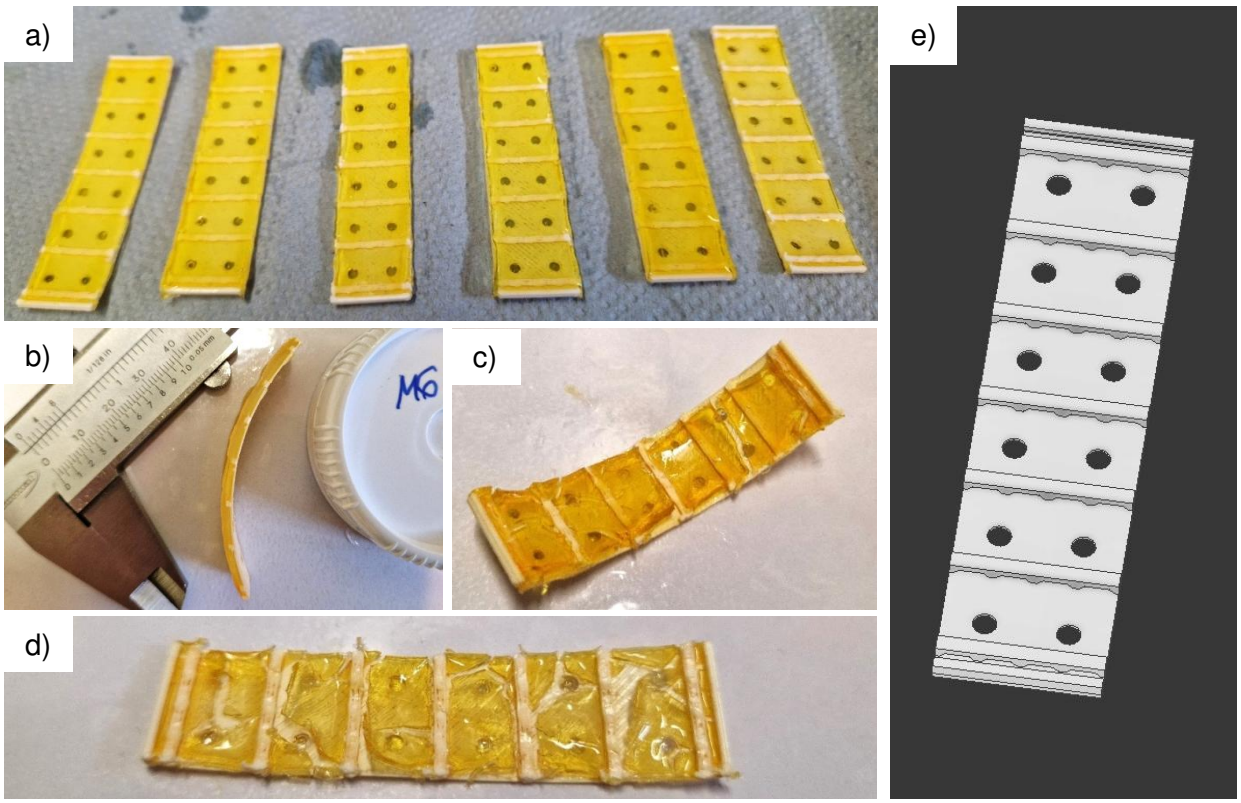



**Fig. 10** Hydrogel-TPU bilayer specimens (The TPU base plates have a nominal as-built length of 60 mm): all samples after printing (a), sample 6 after initial swelling (b), sample 6 after shrinkage (c), sample 3 after shrinkage (d), CAD file of the TPU base plate (0.4 mm × 15 mm × 60 mm) (e)

Reducing the hydrogel layer thickness may therefore represent a promising approach for further optimization, as a lower hydrogel volume could reduce the total contraction force and stored elastic energy generated during constrained shrinkage while potentially retaining sufficient actuation to deform the thin TPU substrate.

## 5. Potential Design Elements for Smart Reactors

### 5.1. Concept and Design Scope

The experimentally demonstrated shrinkage-induced bending of the hydrogel-TPU bilayers provides a basis for considering how such deformation could be translated into functional reactor internals. In contrast to hydrogel components that regulate flow primarily through direct volumetric expansion [37], the investigated multi-material approach allows the responsive hydrogel to act as an actuator while the polymer provides mechanical support and can define the mechanically functional geometry depending on the material arrangement. This enables localized placement of the responsive material, greater geometric freedom, and direct integration of actuation into complex AM structures. Fig. 11 illustrates three potential design elements based on this principle: an adaptive baffle, a variable flow cross-section, and a flow redirecter. These concepts represent an outlook derived from the present material and bilayer experiments; they have not yet been manufactured or experimentally evaluated under flow conditions.

### 5.2. Adaptive Baffles

As shown in Fig. 11a, a hydrogel-polymer bilayer could serve as an adaptive baffle whose orientation changes with the hydrogel state. Shrinkage- or swelling-induced bending could progressively deflect the element into the flow path, thereby changing the local flow trajectory and

potentially enhancing or modifying mixing by altering the degree and direction of flow deflection. In the configuration illustrated in Fig. 11a, the polymer primarily provides mechanical support, while the hydrogel is directly exposed to the process stream. However, the material arrangement could also be inverted, allowing the polymer to define the fluid-contacting geometry while the hydrogel acts as the stimulus-responsive actuator.

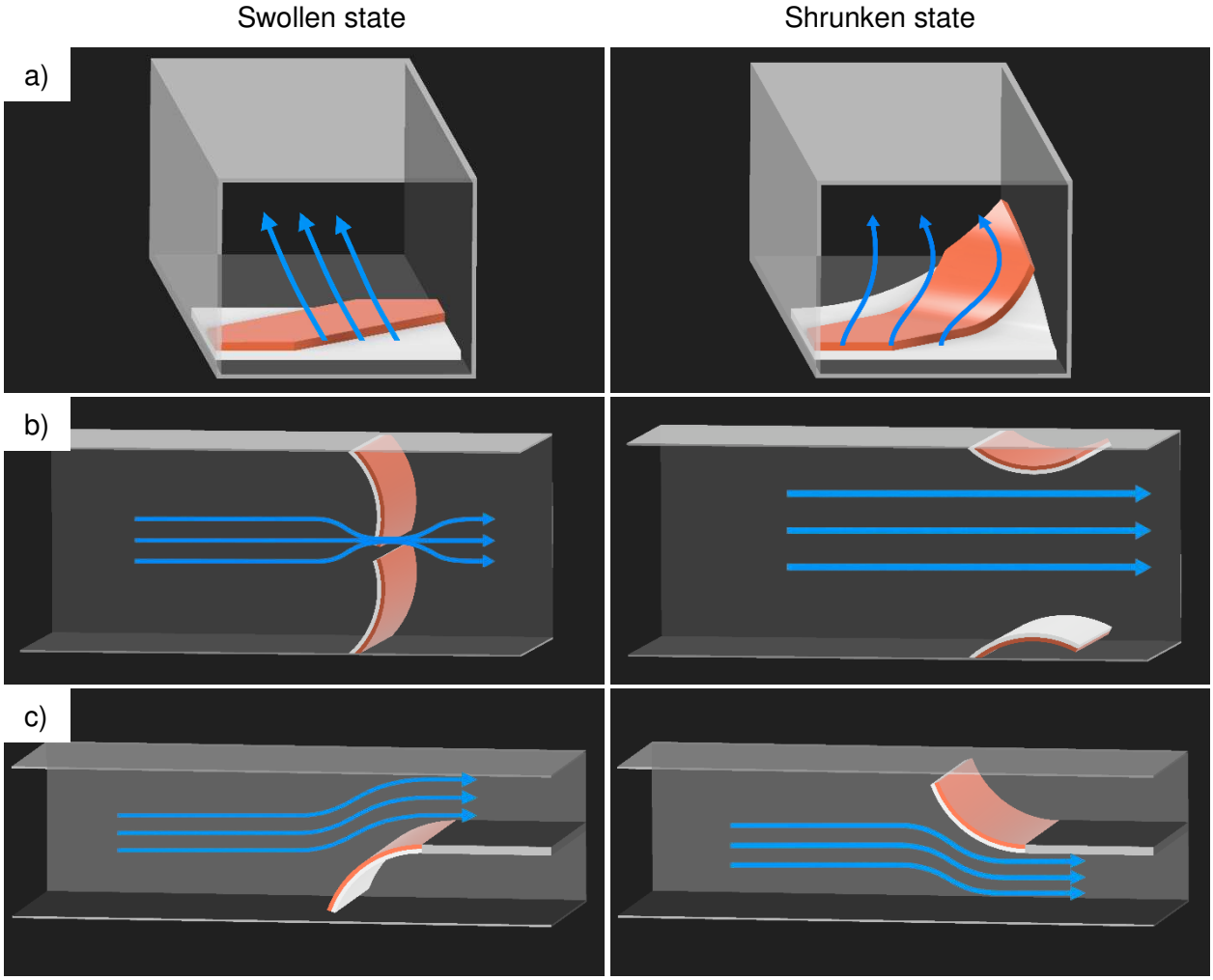



**Fig. 11** Potential hydrogel-polymer bilayer elements for smart reactors integrated into flow channels: adaptive baffle (a), variable flow cross-section (b), flow redirecter (c). The left images show the swollen hydrogel state and the right images the shrunken state. Flow is directed from front to back in the upper pair, from left to right in the lower four images and is visualized with blue arrows. Orange indicates the hydrogel, white the polymer, and gray the flow channel. The blue arrows were generated using ChatGPT (OpenAI) in September of 2026

### 5.3. Variable Flow Cross-Sections and Valves

Fig. 11b illustrates a variable flow cross-section in which opposing bilayer elements deform into or out of the channel. Such deformation could alter the available cross-sectional area and thereby influence local flow velocity, pressure drop, and residence-time distribution. If the elements were designed to close the flow passage completely, the same operating principle would effectively constitute a stimulus-responsive valve. Beyond fluid-dynamic control, the same concept could be used to reversibly expose or withdraw functional surfaces from the process stream. For this purpose, the movable flaps could be designed shorter than those shown schematically in Fig. 11b, allowing them to act primarily as deployable functional surfaces rather than substantially restricting the channel cross-section. Immobilized enzymes, catalysts, or other reactive functionalities could be integrated on these elements. Stimulus-induced deformation could then

vary the effective reactive surface area exposed to the fluid and thereby potentially influence reaction rate and conversion.

### 5.4. Flow Redirecters

A third concept is the flow redirecter shown in Fig. 11c. Its purpose is to autonomously switch the process stream between two downstream channels in response to the hydrogel state of the bilayer flow redirecter. Such a mechanism could, for example, redirect an excessively hot fluid into a cooling loop or divert the stream away from temperature-, pH-, or chemically sensitive functional surfaces when the relevant stimulus exceeds a design-specific threshold. In this way, the bilayer element could act as a locally integrated, stimulus-responsive flow-switching device without requiring external mechanical actuation.

### 5.5. Integration into Adaptive POCS

A further potential application is the integration of localized hydrogel-polymer actuators into complex structured reactor internals such as POCS or triply periodic minimal surfaces (TPMS). Selected struts, junctions, or flexible regions could respond autonomously while the overall structure remains intact, possibly enabling reversible local changes in flow distribution, mixing, pressure drop, and transport characteristics. Multi-material AM could facilitate the direct integration of such responsive regions at predefined locations during fabrication. Geometrically adaptive POCS have also been investigated using interpenetrating structures. Do et al. [38] demonstrated that two interwoven POCS can be displaced relative to each other to adjust internal flow characteristics and pressure drop. Hydrogel-polymer actuators could potentially provide this relative displacement, complementing or replacing external mechanical actuation. Both proposed hydrogel-polymer actuation approaches remain prospective and require experimental validation of the feasibility, achievable deformation, and its effect on reactor performance.

### 5.6. Development Requirements

The concepts shown in Fig. 11 remain to be manufactured and experimentally validated. Their feasibility will depend particularly on the hydrogel-polymer interface, achievable actuation force and displacement, cyclic durability, response kinetics under mechanical constraint, and chemical stability under relevant process conditions. Hydrogel-based flow-control devices are generally subject to trade-offs between gel dimensions, response time, mechanical resilience, and operating conditions [37]. The cracking observed in the present bilayer experiments additionally indicates that anchoring geometry and hydrogel layer thickness require further optimization.

Future work should therefore progress from the simplified bilayer specimens investigated here toward functional baffles, variable flow cross-sections, valves, flow redirecters, and adaptive POCS demonstrators. Their deformation, durability, and actuation force should first be quantified under representative flow conditions before assessing effects on pressure drop, mixing, residence time, transport behavior, reaction rate, or conversion. Such developments could ultimately enable locally or spatially distributed reactor adaptation driven directly by process conditions rather than relying exclusively on external actuators and control loops.

## 6. Conclusion and Outlook

This work demonstrates a multi-material extrusion approach for combining thermoplastics with thermoresponsive hydrogels and transferring hydrogel swelling and shrinkage into structural actuation of polymer-hydrogel bilayers. The printability of two hydrogel formulations with different water contents was systematically investigated using a DoE. For the selected formulation $HG_{hwc}$,

RSM was used to derive a parameter combination that subsequently enabled consistent deposition across the experimental validation runs. However, track width and height remained substantially above their specified targets, highlighting the need to balance dimensional accuracy with extrusion stability, material behavior, and process reliability.

The hydrogel formulation $HG_{hwc}$ exhibited substantial thermoresponsive behavior, with an average unconstrained mass-based shrinkage of 54.22 ± 3.36% between 25 and 40 °C and a characteristic shrinkage timescale on the order of minutes. The bilayer experiments transferred this material response to the structural level, with all six specimens exhibiting a complete reversal in bending direction. At the same time, the experiments identified the hydrogel-polymer interface as a critical design parameter. Insufficient anchoring caused delamination, whereas stronger mechanical interlocking improved deformation transfer but shifted failure toward cohesive cracking of the hydrogel. Successful multi-material actuators therefore require coordinated optimization of material properties, interface design, geometry, curing strategy, and manufacturing parameters.

Based on these findings, potential future applications include adaptive baffles, variable flow cross-sections, valves, flow redirecters, and adaptive POCS with locally integrated responsive regions. Multi-material AM could enable such responsive regions to be spatially integrated into complex 3D structures during fabrication, allowing local or distributed actuation.

Future work should first focus on optimizing the hydrogel formulation, layer thickness, and hydrogel-polymer interface to achieve reliable and repeatable force transfer between the two materials. In parallel, actuation force, cyclic durability, response kinetics under mechanical constraint, and long-term chemical stability should be quantified. The additive manufacturing process should subsequently be extended toward fully three-dimensional multi-material fabrication, including adjacent deposition, thermoplastic deposition onto hydrogel precursor, and alternating material regions across successive layers. Finally, the proposed design elements for smart reactors should be evaluated under representative flow conditions to establish quantitative relationships between stimulus-induced deformation and resulting changes in flow distribution, pressure drop, mixing, transport, and, where applicable, reaction rate and conversion. These developments could ultimately enable smart reactor internals that adapt autonomously to changing process conditions rather than remaining optimized for a single operating state.

## 7. References


[1] L. Ionov, “Biomimetic Hydrogel-Based Actuating Systems,” *Adv Funct Materials*, vol. 23, no. 36, pp. 4555–4570, Sep. 2013, doi: 10.1002/adfm.201203692.

[2] L. Chen, F. Liu, T. Abdiryim, and X. Liu, “Stimuli-responsive hydrogels as promising platforms for soft actuators,” *Materials Today Physics*, vol. 40, p. 101281, Jan. 2024, doi: 10.1016/j.mtphys.2023.101281.

[3] L. Ionov, “Hydrogel-based actuators: possibilities and limitations,” *Materials Today*, vol. 17, no. 10, pp. 494–503, Dec. 2014, doi: 10.1016/j.mattod.2014.07.002.

[4] E. Pei *et al.*, Eds., *Springer Handbook of Additive Manufacturing*. in Springer Handbooks. Cham: Springer International Publishing, 2023. doi: 10.1007/978-3-031-20752-5.

[5] *DIN EN ISO/ASTM 52900:2022-03, Additive Fertigung - Grundlagen - Terminologie (ISO/ASTM 52900:2021); Deutsche Fassung EN ISO/ASTM 52900:2021*. doi: 10.31030/3290011.

[6] S. Peng, Z. Weng, and L. Wu, “Vat photopolymerization 3D printing of hydrogels,” in *Vat Photopolymerization Additive Manufacturing*, Elsevier, 2024, pp. 119–143. doi: 10.1016/B978-0-443-15487-4.00005-4.

[7] F. Zhang *et al.*, “The recent development of vat photopolymerization: A review,” *Additive Manufacturing*, vol. 48, p. 102423, Dec. 2021, doi: 10.1016/j.addma.2021.102423.

[8] X. Hu, C. Spille, M. Schlüter, and I. Smirnova, “Smart Structures—Additive Manufacturing of Stimuli-Responsive Hydrogels for Adaptive Packings,” *Ind. Eng. Chem. Res.*, vol. 59, no. 43, pp. 19458–19464, Oct. 2020, doi: 10.1021/acs.iecr.0c03137.

[9] W. Liu *et al.*, “Enhancing Temperature Responsiveness of PNIPAM Through 3D-Printed Hierarchical Porosity,” *Adv Funct Materials*, vol. 34, no. 41, p. 2403794, Oct. 2024, doi: 10.1002/adfm.202403794.

[10] S. Subedi, S. Liu, W. Wang, S. M. A. Naser Shovon, X. Chen, and H. O. T. Ware, “Multi-material vat photopolymerization 3D printing: a review of mechanisms and applications,” *npj Adv. Manuf.*, vol. 1, no. 1, p. 9, Nov. 2024, doi: 10.1038/s44334-024-00005-w.

[11] Y.-J. Cheng, T.-H. Wu, Y.-S. Tseng, and W.-F. Chen, “Development of hybrid 3D printing approach for fabrication of high-strength hydroxyapatite bioscaffold using FDM and DLP techniques,” *Biofabrication*, vol. 16, no. 2, p. 025003, Apr. 2024, doi: 10.1088/1758-5090/ad1b20.

[12] AMPOWER, “AMPOWER Report 2026,” AMPOWER GmbH & Co. KG, Hamburg, Germany. [Online]. Available: https://additive-manufacturing-report.com/

[13] I. J. Solomon, P. Sevvel, and J. Gunasekaran, “A review on the various processing parameters in FDM,” *Materials Today: Proceedings*, vol. 37, pp. 509–514, 2021, doi: 10.1016/j.matpr.2020.05.484.

[14] AMPOWER, “AMPOWER Report 2025: Market analysis data of calendar year 2024,” AMPOWER GmbH & Co. KG, Hamburg, Germany. [Online]. Available: https://additive-manufacturing-report.com/

[15] S. M. Desai, R. Y. Sonawane, and A. P. More, “Thermoplastic polyurethane for three-dimensional printing applications: A review,” *Polymers for Advanced Techs*, vol. 34, no. 7, pp. 2061–2082, Jul. 2023, doi: 10.1002/pat.6041.

[16] X. Cui *et al.*, “Advances in Extrusion 3D Bioprinting: A Focus on Multicomponent Hydrogel-Based Bioinks,” *Adv Healthcare Materials*, vol. 9, no. 15, p. 1901648, Aug. 2020, doi: 10.1002/adhm.201901648.

[17] D. M. Kirchmajer, R. Gorkin III, and M. in het Panhuis, “An overview of the suitability of hydrogel-forming polymers for extrusion-based 3D-printing,” *J. Mater. Chem. B*, vol. 3, no. 20, pp. 4105–4117, 2015, doi: 10.1039/C5TB00393H.

[18] S. I. Koltsov, T. G. Statsenko, and S. M. Morozova, “Modification of Commercial 3D Fused Deposition Modeling Printer for Extrusion Printing of Hydrogels,” *Polymers*, vol. 14, no. 24, p. 5539, Dec. 2022, doi: 10.3390/polym14245539.

[19] L. Zhou and S. Su, “Design and Validation of a Piston-Driven Syringe-Extrusion Bioprinter Using an FDM Frame,” *Biomimetics*, vol. 10, no. 12, p. 811, Dec. 2025, doi: 10.3390/biomimetics10120811.

[20] P. Imrie and J. Jin, “Multimaterial Hydrogel 3D Printing,” *Macromol. Mater. Eng.*, vol. 309, no. 2, p. 2300272, Feb. 2024, doi: 10.1002/mame.202300272.

[21] X. Hu *et al.*, “Smart reactors – Combining stimuli-responsive hydrogels and 3D printing,” *Chemical Engineering Journal*, vol. 387, p. 123413, May 2020, doi: 10.1016/j.cej.2019.123413.

[22] C. Wang, C. Wang, Z. Huang, and S. Xu, “Materials and Structures toward Soft Electronics,” *Advanced Materials*, vol. 30, no. 50, p. 1801368, Dec. 2018, doi: 10.1002/adma.201801368.

[23] TUHH, “CRC 1615: SMART Reactors for Future Process Engineering,” Technische Universität Hamburg. Accessed: Jul. 23, 2026. [Online]. Available: https://www.tuhh.de/sfb1615/welcome

[24] K. M. Eckert, K. R. Dittmer, S. Setiawan, D. Ohde, A. Liese, and I. Smirnova, “Enzyme Immobilization on Stimuli-Responsive Hydrogels - Part B. Impact of Carrier Responsiveness on Reactor Performance,” *Ind. Eng. Chem. Res.*, vol. 65, no. 26, pp. 13637–13644, Jul. 2026, doi: 10.1021/acs.iecr.6c00960.

[25] J. B. Prettyman and D. T. Eddington, “Leveraging stimuli responsive hydrogels for on/off control of mixing,” *Sensors and Actuators B: Chemical*, vol. 157, no. 2, pp. 722–726, Oct. 2011, doi: 10.1016/j.snb.2011.05.009.

[26] *DIN EN 12254:2012-04, Abschirmungen an Laserarbeitsplätzen - Sicherheitstechnische Anforderungen und Prüfung; Deutsche Fassung EN 12254:2010 + AC:2011*. doi: 10.31030/1873521.

[27] *DIN EN 207:2017-05, Persönlicher Augenschutz - Filter und Augenschutzgeräte gegen Laserstrahlung (Laserschutzbrillen); Deutsche Fassung EN 207:2017*. doi: 10.31030/2631708.

[28] J. Hünting, “Supplementary material to publication with title: Additive Manufacturing of Hydrogel-Polymer Combinations for Applications in Smart Reactors.” www.tore.tuhh.de. doi: 10.15480/882.18028.

[29] G. E. P. Box and K. B. Wilson, “On the Experimental Attainment of Optimum Conditions,” *Journal of the Royal Statistical Society Series B: Statistical Methodology*, vol. 13, no. 1, Jan. 1951, doi: 10.1111/j.2517-6161.1951.tb00067.x.

[30] A. Dean, D. Voss, and D. Draguljić, *Design and Analysis of Experiments*. in Springer Texts in Statistics. Cham: Springer International Publishing, 2017. doi: 10.1007/978-3-319-52250-0.

[31] K. M. Eckert *et al.*, “Enhancing swelling kinetics of pNIPAM lyogels: The role of crosslinking, copolymerization, and solvent,” *Fluid Phase Equilibria*, vol. 597, p. 114462, Oct. 2025, doi: 10.1016/j.fluid.2025.114462.

[32] C. Borgia, D. R. Izquierdo, D. Gabriele, and F. Gagliardi, “Influence of process parameters on shape fidelity in extrusion-based bioprinting: a rheological perspective,” *Int J Adv*

*Manuf Technol*, vol. 143, no. 11–12, pp. 6337–6352, Apr. 2026, doi: 10.1007/s00170-026-17795-2.

[33] M. E. Cooke and D. H. Rosenzweig, “The rheology of direct and suspended extrusion bioprinting,” *APL Bioengineering*, vol. 5, no. 1, p. 011502, Mar. 2021, doi: 10.1063/5.0031475.

[34] P. Rodríguez-Lagar *et al.*, “Effective, versatile and inexpensive extruder system for direct ink writing of high-viscosity pastes,” *Int J Adv Manuf Technol*, vol. 131, no. 9–10, pp. 4739–4753, Apr. 2024, doi: 10.1007/s00170-024-13250-2.

[35] M. Temirel, S. R. Dabbagh, and S. Tasoglu, “Shape Fidelity Evaluation of Alginate-Based Hydrogels through Extrusion-Based Bioprinting,” *JFB*, vol. 13, no. 4, p. 225, Nov. 2022, doi: 10.3390/jfb13040225.

[36] J. P. Reynolds, D. A. Rau, C. B. Williams, and M. J. Bortner, “A rheological method to predict printability of high solids content inks via ultraviolet-assisted material extrusion,” *Additive Manufacturing*, vol. 75, p. 103753, Aug. 2023, doi: 10.1016/j.addma.2023.103753.

[37] A. Beck *et al.*, “Fundamentals of Hydrogel-Based Valves and Chemofluidic Transistors for Lab-on-a-Chip Technology: A Tutorial Review,” *Adv Materials Technologies*, vol. 8, no. 3, p. 2200417, Feb. 2023, doi: 10.1002/admt.202200417.

[38] G. Do, M. Geißelbrecht, W. Schwieger, and H. Freund, “Additive manufacturing of interpenetrating periodic open cellular structures (interPOCS) with in operando adjustable flow characteristics,” *Chemical Engineering and Processing - Process Intensification*, vol. 148, p. 107786, Feb. 2020, doi: 10.1016/j.cep.2019.107786.

## 8. Statements and Declarations

### 8.1. Funding

This project is funded by the Deutsche Forschungsgemeinschaft (DFG, German Research Foundation) – CRC 1615 – 503850735 (subprojects C01, B04, and A01).

### 8.2. Competing Interests

The authors have no relevant financial or non-financial interests to disclose.

### 8.3. Author Contributions

**Jan Hünting:** Conceptualization, Methodology, Software, Validation, Formal analysis, Investigation, Data curation, Writing – original draft, Writing – review & editing, Visualization. **Kathrin Marina Eckert:** Methodology, Resources, Writing – review & editing. **Jelle Jacobs:** Methodology, Validation, Formal analysis, Investigation, Visualization. **Maria Isabelle Maiwald:** Writing – review & editing. **Dirk Herzog:** Conceptualization, Writing – original draft, Writing – review & editing, Supervision, Project administration, Funding acquisition. **Irina Smirnova:** Resources, Writing – review & editing. **Michael Schlüter:** Writing – review & editing. **Ingomar Kelbassa:** Writing – review & editing, Supervision, Project administration, Funding acquisition.

### 8.4. Data Availability

The data that support the findings of this study are openly available in the TUHH Open Research repository TORE (www.tore.tuhh.de) at https://hdl.handle.net/11420/64461 [28].

### 8.5. Use of Generative Artificial Intelligence

During manuscript preparation, ChatGPT (OpenAI) was used for language editing and brainstorming. All AI-assisted suggestions were critically reviewed and verified by the first author. The authors take full responsibility for the final manuscript.

## Supplementary Files

This is a list of supplementary files associated with this preprint. Click to download.

- BilayerbendingAfterFabricationAllSamples.jpg
- BilayerbendingCADTPUbaseplate.jpg
- BilayerbendingChangecurvaturechart.png
- BilayerbendingFullyshrunkenSample1.jpg
- BilayerbendingFullyshrunkenSample2.jpg
- BilayerbendingFullyshrunkenSample3.jpg
- BilayerbendingFullyshrunkenSample4.jpg
- BilayerbendingFullyshrunkenSample5.jpg
- BilayerbendingFullyshrunkenSample6.jpg
- BilayerbendingInitiallyswollenSample1.jpg
- BilayerbendingInitiallyswollenSample2.jpg
- BilayerbendingInitiallyswollenSample3.jpg
- BilayerbendingInitiallyswollenSample4.jpg
- BilayerbendingInitiallyswollenSample5.jpg
- BilayerbendingInitiallyswollenSample6.jpg
- BilayerbendingMATBLAScriptCirclefit.m
- BilayerbendingSignedcurvaturechart.png
- Bilayerbendingresults.xlsx
- HGlwccrystallizedthreads1.jpg
- HGlwccrystallizedthreads2.jpg
- HydrogelDoEresults.xlsx
- Hydrogelformulations.xlsx
- Maineffectcharts.pdf
- ReadMeSupplementaryDataset.pdf
- ShrinkagebehaviorBarchart.png
- ShrinkagebehaviorWaterbath.jpg
- Shrinkagebehaviorresults.xlsx
- ShrinkagekineticsCamerasetup.jpg
- ShrinkagekineticsImagesoftware.jpg
- ShrinkagekineticsMoldprinting.jpg
- ShrinkagekineticsNormalizedvolumechart.png

- ShrinkagekineticsPythoncode.py
- ShrinkagekineticsSamplepositioning.jpg
- StandardizedParetocharts.pdf